GEOLOGY | THE GEOLOGICAL SOCIETY OF AMERICA®

https://doi.org/10.1130/G52661.1

Manuscript received 4 August 2024
Revised manuscript received 26 September 2024
Manuscript accepted 30 October 2024

Published online 13 November 2024

Exploring the impact of deglaciation on fault slip in the Sangre de Cristo Mountains, Colorado, USA

Cecilia Hurtado and Sean F. Gallen*
Department of Geosciences, Colorado State University, Fort Collins, Colorado 80523, USA

ABSTRACT

Few natural examples exist where climate's influence on tectonics is clear. Based on a study of the Sangre de Cristo Mountains in southern Colorado, we argue that climate-driven changes in ice loads affected spatial and temporal slip patterns on the range-front normal fault. Relict glacial features enable the reconstruction of paleoglacier extents and show variable amounts of footwall ice coverage during the Last Glacial Maximum (LGM). Line load models indicate post-LGM ice melting reduced fault clamping stress by ∼20–55 kPa at seismic depths. Flexural isostatic modeling shows several meters of footwall uplift due to ice unloading with spatial patterns and magnitudes consistent with post-LGM fault throw measured from offset Holocene and late Pleistocene alluvial fans. Post-LGM fault throw rates are at least a factor of five higher than middle and early Pleistocene rates. We infer that climate-modulated ice-load changes can pace fault clamping stress and slip patterns on range-bounding normal faults.

INTRODUCTION

Geologists have long been interested in solid earth–climate interactions (Molnar and England, 1990; Willett, 1999). While the impact of mountain building on climate is apparent (Zhisheng et al., 2001; Ehlers and Poulsen, 2009), demonstrating climate's effect on tectonics remains challenging (Whipple, 2009). Studies have explored the impact of orography on convergent orogen kinematics with equivocal results, leading many to infer that tectonic mechanisms dominate system dynamics (Godard et al., 2014; Whipple and Gasparini, 2014). Other studies assessed the role of climate-modulated ice and water loads on fault activity in extensional settings (Hampel and Hetzel, 2006; Hampel et al., 2007, 2021; Larsen et al., 2019). This work demonstrated the potential of climate-paced loading by ice and water bodies to affect fault stress and slip rate. During loading, the lithosphere bends, reducing differential stress, pushing faults further from failure, and depressing slip rates (Figs. 1A and 1B). The reduction in differential stress occurs because flexural stresses elevate the minimum principal stress, σ_3, more so than load-induced increases of the maximum principal stress, σ_1 (Figs. 1A and 1B; Hampel and Hetzel, 2006). When unloaded, the lithosphere rebounds, differential stress increases, and enhanced slip is promoted (Figs. 1A and 1B). However, the only documented example of postglacial slip acceleration is the Teton normal fault (Hampel et al., 2007, 2021).

We explored the hypothesis that deglaciation of the northern Sangre de Cristo Mountains (SCM) affected spatial and temporal slip patterns on the range-front normal fault (Fig. 1C). The SCM are ideal for this investigation because (1) they are a relatively simple normal fault–bounded range, (2) they preserve evidence of Last Glacial Maximum (LGM) glacial extents, (3) the active range-bounding fault offsets Quaternary alluvial fans of various ages, and (4) high-resolution airborne light detection and ranging (LiDAR) data are available (Figs. 1C–1G). We used these attributes to quantify paleoglacial ice loads and their effect on fault clamping stress and footwall isostatic rebound and compare results to vertical fault displacement measurements. Our findings have implications for understanding controls on spatial and temporal patterns of fault slip in the SCM, other glaciated normal fault systems, and the potential for climate to impact tectonics.

Sean F. Gallen https://orcid.org/0000-0002-9288-2850
*Sean.Gallen@colostate.edu

BACKGROUND

The SCM lie in the footwall of the Sangre de Cristo normal fault, an ∼60°WSW-dipping composite fault system in the northern Rio Grande rift (Fig. 1C). The SCM consists primarily of late Paleozoic sedimentary rocks in the center and east and Precambrian granites and gneisses in the west, north, and south (Lindsey, 2010). Their modern topographic expression is associated with Rio Grande rifting. Low-temperature thermochronometry from the footwall and the sediments in the San Luis Basin indicates that rifting began ca. 28–25 Ma with rapid exhumation initiating between ca. 20–10 Ma (Ricketts et al., 2016; Abbey and Niemi, 2020). West-dipping faults in the San Luis Basin accommodate ∼8.2–9.2 km of total displacement (Kluth and Schaftenaar, 1994), and the range-front fault offsets Quaternary alluvial fans (Figs. 1F and 1G; McCalpin, 1982).

The SCM were glaciated during the Quaternary, carving deep U-shape valleys and leaving evidence of LGM ice extents as moraines and trimlines (Figs. 1C–1E). Glaciation peaked at ca. 21–17 ka, deglaciation was rapid between ca. 16 and 14 ka, and modern glaciers are absent today (Refsnider et al., 2009; Leonard et al., 2017, 2023). Quaternary climate change paced both glaciations and alluvial-fan sedimentation; it is inferred that fans formed during cooler intervals (McCalpin, 1982; Ruleman and Brandt, 2021). Primarily based on relative soil development, sedimentologic characteristics, and surface roughness, fans have been assigned to broad age classifications that we adopt here (Ruleman and Brandt, 2021).

Alluvial fans offset by the Sangre de Cristo fault show variable displacement along strike. Trenching indicates that the number of offset-generating earthquakes varies spatially. Radiocarbon and luminescence dating from trenches implies two distinct events at Major Creek at ca. 13–8 ka and ca. 8 ka, and three events at Carr Gulch at ca. 27.5–22.5 ka, ca. 20 ka, and

CITATION: Hurtado, C., and Gallen, S.F., 2024, Exploring the impact of deglaciation on fault slip in the Sangre de Cristo Mountains, Colorado, USA: Geology, v. XX, p. , https://doi.org/10.1130/G52661.1

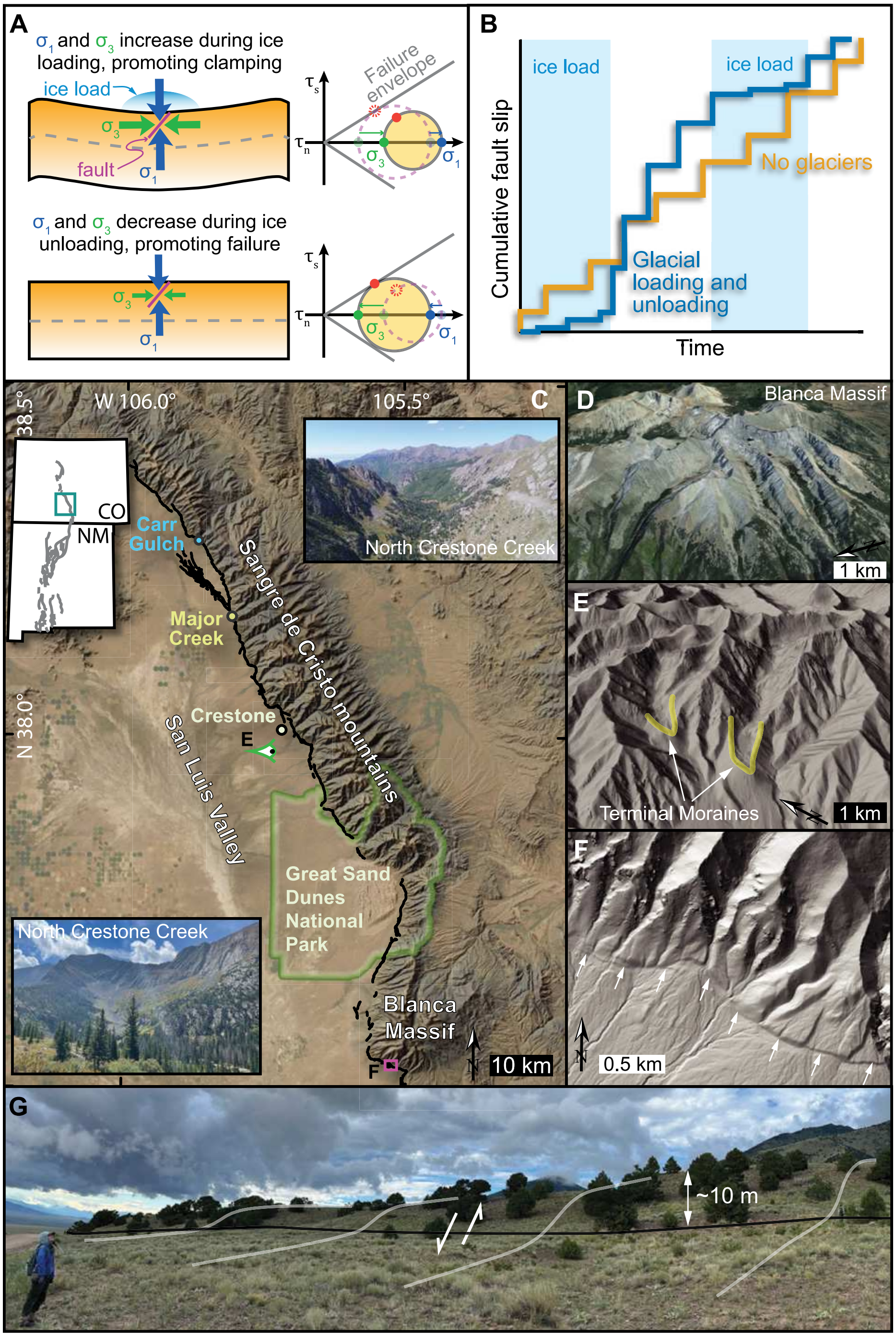

Figure 1. (A) Conceptual models of effects of lithospheric flexure due to ice loading (left) on fault stress in Mohr diagram (right) (after Hampel and Hetzel, 2006). During loading, flexure reduces differential stress by increasing σ_3 relative to σ_1, pushing fault away from failure, and opposite occurs during unloading. τ_s and τ_n are shear and normal stress, respectively. (B) Schematic fault-slip variations for system with (blue) and without (orange) changing ice loads. (C) Satellite map of Sangre de Cristo Mountains (SCM) with black line showing bounding fault. Inset map (top left) shows location of SCM (green box) in context of Rio Grande rift faults (gray lines); CO—Colorado; NM—New Mexico. Inset photos are from drainage just north of Crestone, Colorado. (D) Google Earth™ image showing glacial features. (E) Perspective view showing terminal moraines (view from green eye in C). (F) Hillshade image showing Quaternary fault scarp (location is purple box in C). (G) Field photo of fault scarp in alluvium north of Crestone.

ca. 8 ka (Fig. 1C; McCalpin, 1982; McCalpin and Kirkham, 2006). Estimated earthquake recurrence intervals are 5–50 k.y., and Quaternary slip rates are ≤0.2 mm yr^{-1} (McCalpin, 1982; McCalpin et al., 2011). These values are on the lower end of long-term horizontal extension rates estimated for the northern Rio Grande rift (0.1–1.5 mm yr^{-1}; Murray et al., 2019) and San Luis Basin (0.1–1.1 mm yr^{-1}; van Wijk et al., 2018).

METHODS

Ice Reconstruction

We reconstructed LGM ice extent using the paleoglacier reconstruction (GLaRe) model (Pellitero et al., 2016). GLaRe approximates an equilibrium glacial valley profile along the flow centerline using plastic rheology, local valley slope, and ice density, assuming a basal shear stress of 100 kPa and a shape factor related to valley cross-sectional geometry (see Supplemental Material for details[1]). We implemented GlaRe in Matlab, building on TopoToolbox (Schwanghart and Scherler, 2014). We identified glacial valleys on the east and west sides of the SCM from topographic data and satellite imagery (Figs. 1D and 1E) and used TopoToolbox to select glacial valley centerlines. For each valley, we defined the lower boundary condition as the intersection of the centerline and terminal moraines where preserved and the transition from U-shaped to V-shaped valley elsewhere. We calculated glacial centerline heights and interpolated them to valley walls to approximate a two-dimensional (2-D) glacial surface. We iteratively adjusted the shape factor in each valley until there was correspondence between the modeled glacial surface and lateral moraines and trimlines.

Stress Modeling

We explored the impact of ice unloading on range-front fault clamping stress using a one-dimensional (1-D) line load model (Jaeger et al., 2007; see Supplemental Material for details). This model assumes an elastic half-space to predict stress change on a fault of a given dip striking perpendicular to the load. Ice-load thickness and extent perpendicular to the fault were estimated based on 5-km-wide swath profiles of the ice reconstructions, which we used to determine the line load based on the average load thickness and width, assuming typical glacial ice density. We modeled stress change resolved onto the trace of a 60°W-dipping fault, which was converted to unclamping stress assuming Coulomb failure and a coefficient of friction of 0.6 (Gallen and Thigpen, 2018).

Flexural Isostasy

We modeled the flexural-isostatic response to ice unloading using a 2-D infinite elastic plate model (Watts, 2001). The ice-load magnitude and extent, assumed ice and mantle densities (920 km m^{-3} and 3300 km m^{-3}, respectively), and the lithospheric rigidity, approximated by the effective elastic thickness, T_e, determined the isostatic response.

[1]Supplemental Material. Extended methods, supplemental figures, and supporting citations. Please visit https://doi.org/10.1130/GEOL.S.27473175 to access the supplemental material; contact editing@geosociety.org with any questions.

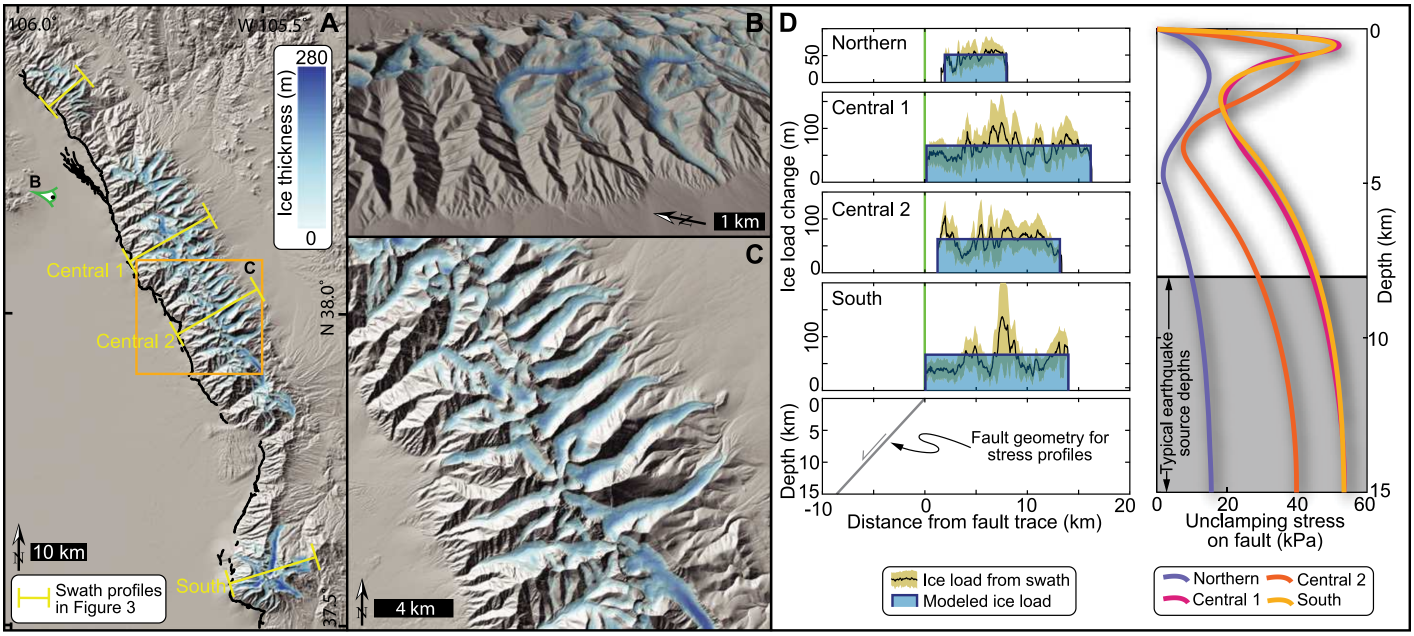

Figure 2. (A) Ice reconstructions over hillside image with mapped fault (black line) and locations of panels B and C and swath profiles in D. (B) Perspective view of ice reconstructions. (C) Zoom-in of ice reconstructions in central Sangre de Cristo Mountains (SCM). (D) Left panel shows swath profiles of change in ice load and simplified line load approximations with reference to fault surface trace (green line) and assumed fault geometry. Right panel shows unclamping magnitudes resolved along assumed fault.

We assumed a T_e of 5 km and 2 km based on a regional analysis of topographic deflections along the northern Rio Grande rift (Peterson and Roy, 2005) and our analysis of footwall deflection in the SCM, respectively (see Supplemental Material for details). To approximate a broken plate, we mirrored the load across the fault, calculated flexure on both sides, and removed the response on the hanging wall. This approximation mimics 1-D broken plate flexure in the middle of the fault while accounting for along-strike lithospheric rigidity away from the fault center.

Fault Mapping and Scarp Offsets

We used 1-m-resolution bare-earth LiDAR data to map the surface expression of the Sangre de Cristo fault at the 1:4,400 scale (see Supplemental Material for details). Mapped fault traces were based on inspection of the LiDAR data and topographic derivatives (e.g., hillshade, slope, and curvature). To quantify vertical scarp offset, we extracted 579 topographic profiles perpendicular to the local fault strike. Nearly all profiles were simple steps, allowing projections of linear regression above and below scarps to determine the vertical offset. From these measurements, we calculated the vertical separation by considering fan slope and fault dip to more accurately determine throw (see Supplemental Material for details; Caskey, 1995; Hampel et al., 2021).

Most fault scarps cut Quaternary alluvial fans, enabling approximation of the time scale over which vertical fault displacement accrued. We classified alluvial fans into three age groups based on the best available maps of the area (1:75,000 scale) and ages inferred by Ruleman and Brandt (2021): early-to-middle Pleistocene (2588–129 ka), late Pleistocene (129–11.7 ka), and Holocene (<11.7 ka). We also included offsets in bedrock and assumed they record displacement since at least the early Pleistocene (2588–788 ka). The coarse scale of the alluvial-fan mapping and age associations contributed this study's largest source of uncertainty.

RESULTS

The paleoglacier reconstructions show that glaciation affected three higher-elevation sections of the SCM, separated by two unglaciated segments (Figs. 2A–2C). Modeled ice loads are 62 ± 42 m ($\mu \pm 1\sigma$) thick. Our ice reconstructions in the Blanca Massif are consistent with sophisticated models that consider climate and hydrological mass balance, giving confidence in our reconstructions (Brugger et al., 2021). Swath profiles extracted from the glaciated sections indicate ice loads were ~50–70 m thick and ~5–15 km wide (Fig. 2D). Line load models of the ice unloading suggest that deglaciation reduced downdip fault clamping stress by ~20–55 kPa at depths of ~8–15 km (Fig. 2D). Flexural isostatic deflection is greatest at the fault center, with maximum values of ~3–5 m, depending on assumed T_e and taper to the fault tips (Figs. 3A and 3B). A second-order, shorter-wavelength deflection pattern shows local highs in glacial segments, with the higher T_e models exhibiting a smoother deflection pattern (Figs. 2A, 3A, and 3B).

Fault mapping shows a composite fault system with a relatively simple large-scale geometry (Figs. 1C and 3C), with one exception: a series of faults, known as the "Villa Grove Swarm" between Carr Gulch and Major Creek, which strike NW away from the main fault trace at a relay zone (Fig. 1C). Fault throw ranges between ~0.66 and 35 m (6.1 ± 5.2 m, $\mu \pm 1\sigma$), with higher throw in the center of formerly glaciated segments and the highest offsets in the center of the range (Figs. 3D and 4A). We calculated time-averaged throw rates for scarps in Quaternary alluvial fans. To be conservative, we used maximum age estimates for Holocene rates and minimum ages for middle (-to-early) Pleistocene rates; we assumed late Pleistocene fans were abandoned during the LGM at ca. 25 ka. We included bedrock offsets and conservatively assumed that they record displacement since at least the early Pleistocene. Rates are faster for shorter integrated time scales, with median (+75th/–25th percentiles) Holocene rates of 0.316 (+0.256/–0.082) mm yr^{-1} and late, middle, and early Pleistocene rates of 0.168 (+0.129/–0.068), 0.034 (+0.028/–0.015), and 0.008 (+0.003/–0.003) mm yr^{-1}, respectively (Fig. 4B).

DISCUSSION AND CONCLUSIONS

Modeling shows LGM deglaciation of the SCM reduced range-front fault clamping stress by ~20–55 kPa at depths where most seismic activity is observed today (Fig. 2D; Bell, 2020). Flexural isostatic rebound at the fault trace approximates fault-scarp throw magnitudes and along-strike patterns, where the low T_e models closely mimic postglacial (Holocene and late Pleistocene) throw (Fig. 4A). Postglacial throw rates are conservatively estimated to be at least a factor of five higher than middle and early Pleistocene rates (Fig. 4B). These results are compelling evidence that ice

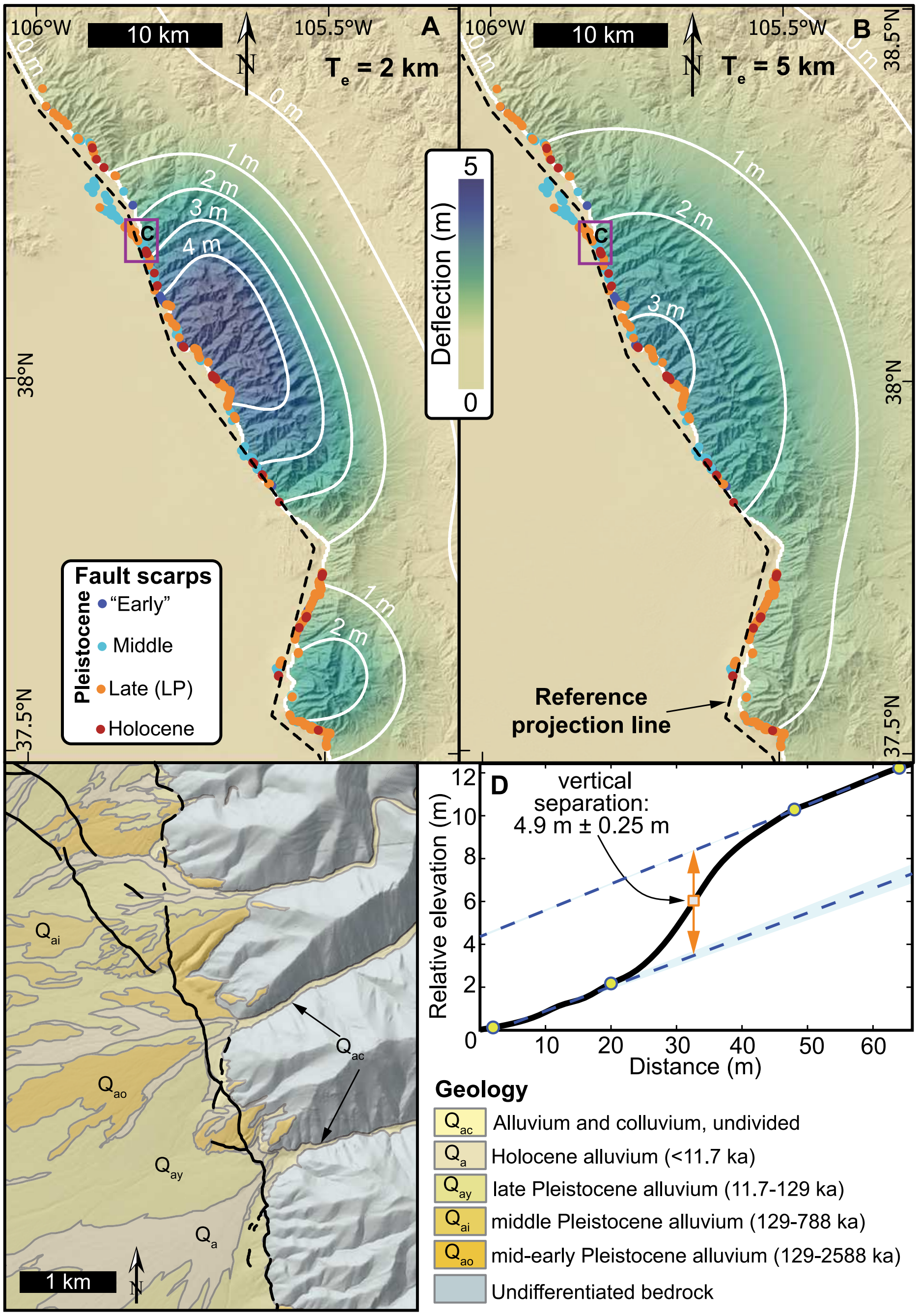

Figure 3. (A, B) Flexural isostatic rebound for different effective elastic thickness (T_e) values, with locations of 597 profiles used to calculate scarp offset colored by Quaternary unit age from Ruleman and Brandt (2021) (see Supplemental Material for details [see text footnote 1]). Note early Pleistocene is in quotes because measurements are from scarps in bedrock, which are assumed to be at least this old. Dashed black line is used to project fault-scarp offset and flexural results across range shown in Figure 4. (C) Zoom-in of mapped fault and alluvial fans (Ruleman and Brandt, 2021) near Major Creek (location shown by purple box in A and B). (D) Typical scarp profile (black line) and linear regression projections (dashed blue lines) ± 1σ (blue shading) used to determine scarp vertical separation, from which vertical fault offset was calculated after Caskey (1995), as detailed in Supplemental Material.

melting in the SCM affected the spatial and temporal patterns of fault stress and slip.

It might be argued that fault segments with the highest long-term slip rates produce the highest topography and are more likely to be occupied by glaciers, so the correspondence between high throw rates and glaciers is coincidental. However, this argument does not mean glaciers do not modulate fault stress and activity, and it is difficult to explain the increase in slip rates over shorter integrated time scales in this context (Fig. 4B). Enhanced post-LGM rates could be a "Sadler effect" (Sadler, 1981), yet short-term perturbations to a long-term average produce the Sadler effect (Fig. 1B; Nicol et al., 2009). When fault-slip rate varies about a long-term average, short-term rates are a function of the integration time scale and whether one measures the rate during a slow-slip or rapid-slip phase (Fig. 1B). Thus, the increase in throw rate determined here is likely due to actual post-LGM fault-slip-rate acceleration.

Our results suggest that deglaciation of the SCM unclamped the Sangre de Cristo fault and affected spatial and temporal slip patterns. Long-term tectonic extension dominates spatial and temporal slip patterns, but our results support the notion that climate, via glacial advance and retreat, can affect fault-slip variability, implying that earthquakes can be clustered in space and time. Differential stress drops on faults when loaded, allowing more elastic strain accumulation during glaciation due to slow, persistent tectonically driven extension. When ice melts, differential stress increases, allowing accelerated postglacial fault-slip and earthquake activity (Hampel and Hetzel, 2006; Hampel et al., 2007, 2021). This interpretation emphasizes that climate-driven hydrologic cycle perturbations should be considered when interpreting fault-slip and earthquake recurrence interval data. It is possible that tectonically active regions experiencing rapid changes in ice and water loads due to recent and ongoing climate change could experience elevated fault activity due to changing boundary conditions.

ACKNOWLEDGMENTS

C. Hurtado thanks the Geological Society of America Graduate Student Research Grants Program (#13445-22), Four Corners Geological Society (2022 Master's thesis grant), and Colorado State University Warner College of Natural Resources for financial support. S.F. Gallen acknowledges National Science Foundation EAR grants 2041910 and 2139894 for partial support. We thank A. Hampel, E. Leonard, and an anonymous reviewer for their constructive reviews, M. Schwarz, S. Johnstone, J. Thompson-Jobe, N. Reitman, J. Singleton, S. Denning, and D. McGrath for valuable discussions, and S. Malavarca, E. Perman, and S. Slonkosky for field assistance.

REFERENCES CITED

Abbey, A.L., and Niemi, N.A., 2020, Perspectives on continental rifting processes from spatiotemporal patterns of faulting and magmatism in the Rio Grande rift, USA: Tectonics, v. 39, https://doi.org/10.1029/2019TC005635.

Bell, J., 2020, Seismic Activity in the Northern Sangre de Cristo Fault Zone [M.S. thesis]: Boulder, Colorado, University of Colorado at Boulder, 61 p., https://www.proquest.com/docview/2420687477/abstract/2FC2127267CA4E67PQ/1 (accessed March 2024).

Brugger, K.A., Leonard, E.M., Refsnider, K.A., and Dolan, P., 2021, Climate on the Blanca Massif, Sangre de Cristo Mountains, Colorado, USA, during the Last Glacial Maximum: Quaternary, v. 4, https://doi.org/10.3390/quat4030027.

Caskey, S.J., 1995, Geometric relations of dip slip to a faulted ground surface: New nomograms for estimating components of fault displacement: Journal of Structural Geology, v. 17, p. 1197–1202, https://doi.org/10.1016/0191-8141(95)00023-7.

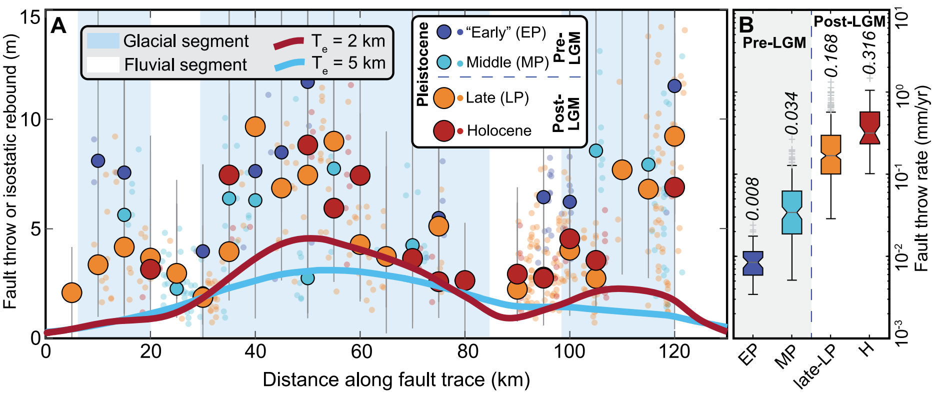

Figure 4. (A) Across-strike patterns for fault throw and flexural rebound. Small transparent dots are measured scarp data. Large solid dots are 5 km binned median values, and gray lines are 75th to 25th percentile ranges. Solid lines show modeled flexural isostatic rebound at range front for different effective elastic thickness (*T_e*) values. LGM—Last Glacial Maximum. (B) Box plot of inferred fault throw rates for different alluvial-fan age groups. Median values are in italics, and box limits are 75th to 25th percentiles.

Ehlers, T.A., and Poulsen, C.J., 2009, Influence of Andean uplift on climate and paleoaltimetry estimates: Earth and Planetary Science Letters, v. 281, p. 238–248, https://doi.org/10.1016/j.epsl.2009.02.026.

Gallen, S.F., and Thigpen, J.R., 2018, Lithologic controls on focused erosion and intraplate earthquakes in the Eastern Tennessee seismic zone: Geophysical Research Letters, v. 45, p. 9569–9578, https://doi.org/10.1029/2018GL079157.

Godard, V., Bourlès, D.L., Spinabella, F., Burbank, D.W., Bookhagen, B., Fisher, G.B., Moulin, A., and Léanni, L., 2014, Dominance of tectonics over climate in Himalayan denudation: Geology, v. 42, p. 243–246, https://doi.org/10.1130/G35342.1.

Hampel, A., and Hetzel, R., 2006, Response of normal faults to glacial-interglacial fluctuations of ice and water masses on Earth's surface: Journal of Geophysical Research: Solid Earth, v. 111, https://doi.org/10.1029/2005JB004124.

Hampel, A., Hetzel, R., and Densmore, A.L., 2007, Postglacial slip-rate increase on the Teton normal fault, northern Basin and Range Province, caused by melting of the Yellowstone ice cap and deglaciation of the Teton Range?: Geology, v. 35, p. 1107–1110, https://doi.org/10.1130/G24093A.1.

Hampel, A., Hetzel, R., and Erdmann, M.-S., 2021, Postglacial slip distribution along the Teton normal fault (Wyoming, USA), derived from tectonically offset geomorphological features: Geosphere, v. 17, p. 1517–1533, https://doi.org/10.1130/GES02370.1.

Jaeger, J., Cook, N.G., and Zimmerman, R., 2007, Fundamentals of Rock Mechanics: Malden, Massachusetts, Wiley-Blackwell, 488 p.

Kluth, C.F., and Schaftenaar, C.H., 1994, Depth and geometry of the northern Rio Grande rift in the San Luis Basin, south-central Colorado, *in* Keller, G.R., and Cather, S.M., eds., Basins of the Rio Grande Rift: Structure, Stratigraphy, and Tectonic Setting: Geological Society of America Special Paper 291, p. 27–37, https://doi.org/10.1130/SPE291-p27.

Larsen, D.J., Crump, S.E., Abbott, M.B., Harbert, W., Blumm, A., Wattrus, N.J., and Hebberger, J.J., 2019, Paleoseismic evidence for climatic and magmatic controls on the Teton fault, WY: Geophysical Research Letters, v. 46, p. 13,036–13,043, https://doi.org/10.1029/2019GL085475.

Leonard, E.M., Laabs, B.J.C., Plummer, M.A., Kroner, R.K., Brugger, K.A., Spiess, V.M., Refsnider, K.A., Xia, Y., and Caffee, M.W., 2017, Late Pleistocene glaciation and deglaciation in the Crestone Peaks area, Colorado Sangre de Cristo Mountains, USA—Chronology and paleoclimate: Quaternary Science Reviews, v. 158, p. 127–144, https://doi.org/10.1016/j.quascirev.2016.11.024.

Leonard, E.M., Laabs, B.J.C., Marcott, S.A., Crawford, E.E., Mackall, B.T., Ibarra, D.E., Osman, M.B., Plummer, M.A., and Caffee, M.W., 2023, Chronology and climate of the Last Glacial Maximum and the subsequent deglaciation in the northern Medicine Bow Mountains, Wyoming, USA: Quaternary Science Advances, v. 12, https://doi.org/10.1016/j.qsa.2023.100109.

Lindsey, D.A., 2010, The Geologic Story of Colorado's Sangre de Cristo Range: U.S. Geological Survey Circular 1349, 14 p., https://doi.org/10.3133/cir1349.

McCalpin, J.P., 1982, Quaternary geology and neotectonics of the west flank of the northern Sangre de Cristo Mountains, south-central Colorado: Colorado School of Mines Quarterly, v. 77, p. 1–97.

McCalpin, J.P., and Kirkham, R.M., 2006, Refine Slip Rates and Segmentation of the Northern Sangre de Cristo Fault, Colorado's Largest Active Fault: Crestone, Colorado, submitted to the U.S. Geological Survey by GEO-HAZ Consulting, Inc., Unpublished Final Technical Report, 42 p.

McCalpin, J.P., Harrison, J.B.J., Berger, G.W., and Tobin, H.C., 2011, Paleoseismicity of a low-slip-rate normal fault in the Rio Grande rift, USA: The Calabacillas fault, Albuquerque, New Mexico, *in* Audemard M., F.A., Michetti, A.M., and McCalpin, J.P., eds., Geological Criteria for Evaluating Seismicity Revisited: Forty Years of Paleoseismic Investigations and the Natural Record of Past Earthquakes: Geological Society of America Special Paper 479, p. 23–46, https://doi.org/10.1130/2011.2479(01).

Molnar, P., and England, P., 1990, Late Cenozoic uplift of mountain ranges and global climate change: Chicken or egg?: Nature, v. 346, p. 29–34, https://doi.org/10.1038/346029a0.

Murray, K.D., Murray, M.H., and Sheehan, A.F., 2019, Active deformation near the Rio Grande rift and Colorado Plateau as inferred from continuous global positioning system measurements: Journal of Geophysical Research: Solid Earth, v. 124, p. 2166–2183, https://doi.org/10.1029/2018JB016626.

Nicol, A., Walsh, J., Mouslopoulou, V., and Villamor, P., 2009, Earthquake histories and Holocene acceleration of fault displacement rates: Geology, v. 37, p. 911–914, https://doi.org/10.1130/G25765A.1.

Pellitero, R., Rea, B.R., Spagnolo, M., Bakke, J., Ivy-Ochs, S., Frew, C.R., Hughes, P., Ribolini, A., Lukas, S., and Renssen, H., 2016, GlaRe, a GIS tool to reconstruct the 3D surface of palaeoglaciers: Computers & Geosciences, v. 94, p. 77–85, https://doi.org/10.1016/j.cageo.2016.06.008.

Peterson, C., and Roy, M., 2005, Gravity and flexure models of the San Luis, Albuquerque, and Tularosa basins in the Rio Grande rift, New Mexico, and southern Colorado, *in* Lucas, S.G., Zeigler, K.E., Lueth, V.W., and Owen, D.E., eds., Geology of the Chama Basin: Socorro, New Mexico, New Mexico Geological Society, 56th Field Conference, p. 105–114, https://doi.org/10.56577/FFC-56.105.

Refsnider, K.A., Brugger, K.A., Leonard, E.M., McCalpin, J.P., and Armstrong, P.P., 2009, Last Glacial Maximum equilibrium-line altitude trends and precipitation patterns in the Sangre de Cristo Mountains, southern Colorado, USA: Boreas, v. 38, p. 663–678, https://doi.org/10.1111/j.1502-3885.2009.00097.x.

Ricketts, J.W., Kelley, S.A., Karlstrom, K.E., Schmandt, B., Donahue, M.S., and van Wijk, J., 2016, Synchronous opening of the Rio Grande rift along its entire length at 25–10 Ma supported by apatite (U-Th)/He and fission-track thermochronology, and evaluation of possible driving mechanisms: Geological Society of America Bulletin, v. 128, p. 397–424, https://doi.org/10.1130/B31223.1.

Ruleman, C.A., and Brandt, T.R., 2021, Surficial Geology of the Northern San Luis Valley, Saguache, Fremont, Custer, Alamosa, Rio Grande, Conejos, and Costilla Counties, Colorado: U.S. Geological Survey Scientific Investigations Map 3475, 2 sheets, https://doi.org/10.3133/sim3475.

Sadler, P.M., 1981, Sediment accumulation rates and the completeness of stratigraphic sections: The Journal of Geology, v. 89, p. 569–584, https://doi.org/10.1086/628623.

Schwanghart, W., and Scherler, D., 2014, Short Communication: TopoToolbox 2–MATLAB–based software for topographic analysis and modeling in Earth surface sciences: Earth Surface Dynamics, v. 2, p. 1–7, https://doi.org/10.5194/esurf-2-1-2014.

van Wijk, J., Koning, D., Axen, G., Coblentz, D., Gragg, E., and Sion, B., 2018, Tectonic subsidence, geoid analysis, and the Miocene–Pliocene unconformity in the Rio Grande rift, southwestern United States: Implications for mantle upwelling as a driving force for rift opening: Geosphere, v. 14, p. 684–709, https://doi.org/10.1130/GES01522.1.

Watts, A.B., 2001, Isostasy and Flexure of the Lithosphere: Cambridge, UK, Cambridge University Press, 508 p.

Whipple, K.X., 2009, The influence of climate on the tectonic evolution of mountain belts: Nature Geoscience, v. 2, p. 97–104, https://doi.org/10.1038/ngeo413.

Whipple, K.X., and Gasparini, N.M., 2014, Tectonic control of topography, rainfall patterns, and erosion during rapid post–12 Ma uplift of the Bolivian Andes: Lithosphere, v. 6, p. 251–268, https://doi.org/10.1130/L325.1.

Willett, S.D., 1999, Orogeny and orography: The effects of erosion on the structure of mountain belts: Journal of Geophysical Research: Solid Earth, v. 104, p. 28,957–28,981, https://doi.org/10.1029/1999JB900248.

Zhisheng, A., Kutzbach, J.E., Prell, W.L., and Porter, S.C., 2001, Evolution of Asian monsoons and phased uplift of the Himalaya–Tibetan Plateau since late Miocene times: Nature, v. 411, p. 62–66, https://doi.org/10.1038/35075035.

Printed in the USA

Supplementary materials

Title: Exploring the impact of deglaciation on fault slip in the Sangre de Cristo Mountains, Colorado

Authors: Cece Hurtado and Sean F. Gallen

Affiliation: Colorado State University, Department of Geosciences

Extended Methods:

Ice reconstructions

Quantifying the load on the Sangre de Cristo Mountains due to glaciers required reconstruction of glacial extents in the drainage basins affected by glaciers. Based on the basin geometries left behind by glacial erosion, it is clear that the alpine glaciers that inhabited the valleys had large asymmetries between the east and west sides of the range. On the east side of the range, the glaciers tend to be consistently narrow and linear, whereas, on the west side, the glaciers have more varying geometries and tend to cover more area.

The glacial extent reconstruction process was adapted from the equations and workflow in the Pellitero et al. (2016) ArcMap-based GlaRe toolbox (Figure S1). This toolbox allows the user to recreate the 3D surface of a land-terminating paleo-glacier by calculating ice thickness along the main flow lines of the glacier. Using a DEM of the modern topography for the bed slope, a user-defined input for the terminus of the glacier, and a user-defined input identifying the channel head locations, GlaRe uses a derivation of the shear stress equation:

$$\tau = \rho g H sin(\alpha) \qquad (1)$$

where τ is the basal shear stress, ρ is the density of glacial ice, g is the acceleration due to gravity, H is the thickness of the glacier in meters, and α is the surface slope of the glacier. The derivation of this equation to calculate glacier height, H, at nodes spaced along the main channel of the glacier, GlaRe utilizes an iterative process put forth by Shilling and Hollin (1981):

$$h_{i+1} = h_i + \frac{\tau_{av}}{F\rho g}\frac{\Delta x}{H_i} \qquad (2)$$

where h is the elevation of the glacier surface, i is the node number moving up valley from the terminus node, iteration number, τ_{av} is the basal shear stress, F is the shape factor, and Δx is the length between nodes to recreate a one-dimensional representation of the glacier profile. Ice typically cannot tolerate shear stresses exceeding 150 kPa, but will not deform under stresses less than 50 kPa, therefore, an average of 100 kPa was used for each glacial reconstruction presented here (Pierce, 1979; Bennett and Glasser, 2010; Pellitero et al., 2016). The shape factor, F, was designed to account for the lateral drag that valley glaciers encounter. The shape factor is calculated by the following equation by Benn and Hulton (2010):

$$F = \frac{A}{Hp} \qquad (3)$$

where *A* is the cross-sectional area, and *p* is the length of the intersection of the cross-sectional area and the underlying glacier bed. The *F*-factor decreases with increasing constriction, therefore, an *F*-factor of 1 is best suited to an ice field or an ice cap, which is not constrained by the topography, whereas valley glacier F-factors can vary between 0.7–0.9 (Jiskoot, 2011) (Figure S2). In the reconstructions for this work, the *F*-factor values were constrained by both erosional and depositional evidence observed in satellite and lidar imagery.

We coded these equations in Matlab and used them in tandem with TopoToolbox v2 (Schwanghart and Scherler, 2014) functions to reconstruct glacier profiles for every drainage that had depositional and/or erosional evidence of glaciation (Figures 1, 2, S1). With the glacial profiles and topographic constraints, we interpolated a two-dimensional glacial ice surface using standard *griddata* and *meshgrid* Matlab functions (Figure S1). Glacier termini were approximated using preserved terminal moraines where available or alternatively locations where the valley morphology changes from U-shaped to V-shaped. In total, 24 glacial reconstructions were completed for the west side, and 34 glacial reconstructions were completed for the east side (Figure 2).

Stress modeling

We quantified the amount of stress along the dipping fault trace due to the various removal ice loads by utilizing an analytical line load model (Jaeger et al., 2007). The two-dimensional stress components τ_{xx} and τ_{zz} at a given point caused by a distributed line load N_o, referenced to the θ_1 and θ_2 angles from the load edges (measured clockwise from the positive *x* direction, *z* is the positive downward direction) (Figure S3):

$$\tau_{xx} = \frac{N_o}{2\pi a}[(\theta_1 - \theta_2) + \sin(\theta_1 - \theta_2)\cos(\theta_1 + \theta_2)] \quad (4)$$

$$\tau_{zz} = \frac{N_o}{2\pi a}[(\theta_1 - \theta_2) - \sin(\theta_1 - \theta_2)\cos(\theta_1 + \theta_2)] \quad (5)$$

$$\tau_{xz} = \frac{N_o}{2\pi a}[\sin(\theta_1 - \theta_2)\sin(\theta_1 + \theta_2)] \quad (6)$$

where *a* is half of the width of the load. The shear stress, τ_s, and normal stress, τ_n, elements on the fault plane can then be solved for, with dip angle φ on a strike perpendicular to the *xz* plane (Figure S3):

$$\tau_s = (\tau_{zz} - \tau_{xx})\sin(\varphi)\cos(\varphi) + \tau_{xz}(cos^2(\varphi) - \sin^2(\varphi)) \quad (7)$$

$$\tau_n = \tau_{zz}cos^2(\varphi) - 2\tau_{xz}\sin(\varphi)\cos(\varphi) + \tau_{xx}sin^2(\varphi) \quad (8)$$

If a line perpendicular to the general strike of the Sangre de Cristo fault is chosen, we can calculate the unclamping stress on the fault by assuming a dip angle of 60° for the fault if the coefficient of friction, pore-fluid pressure, and cohesion do not vary significantly over time:

$$\Delta\sigma_c = \Delta|\tau_s| + \mu\Delta\tau_n \quad (9)$$

where $\Delta\sigma_c$ is the change in Coulomb stress (termed the unclamping stress), and μ is the coefficient of friction. Using techniques put forth by Jaeger et al. (2007) and Amos et al. (2014), we can model the stress changes with line load distributions reproducing the elastic response of the lithosphere to the various loads (Figure S3). We calculate the change in stress in four different glaciated sections of the Sangre de Cristo Mountains resolved onto a 60° west-dipping fault plane. We are most interested in stress change at depths between 8 and 15 km because previous studies estimate this depth range is where most historic earthquake nucleation occurs in Basin and Range (Doser and Smith, 1989) and near the Blanca Massif (Bell, 2020).

Flexural Isostasy

The objective for the flexural isostasy modeling was to estimate the expected deflection of the lithosphere in response to the removal of the eroded loads (both the maximum and the minimum to provide the upper and lower bounds) from the footwall, the removal of the glacial load from the footwall, and the addition of the depositional load on the hanging wall. We chose an elastic model as opposed to a viscoelastic model for the isostatic response estimations to simplify the calculation and retain similar assumptions between the isostasy model and the line load stress modeling. For the erosional unloading, the viscous relaxation time for the asthenosphere is well within the timeline of erosion of the footwall and deposition of the hanging wall (~10^4 yrs), so the elastic model is appropriate over these longer timescales. However, we acknowledge that the glacial unloading period is closer to the asthenospheric viscous relaxation timescale, and thus interpret my ice unloading isostatic rebound estimates as maximum deflection estimates.

We used a 2D infinite plate elastic half-space model to simulate the flexural isostatic response to a surface load change as (Watts, 2001):

$$q = D\frac{d^4w}{dx^4} + \Delta\rho g w \quad (10)$$

where q is the surface load, D is the lithospheric rigidity, w is the vertical plate deflection, $\Delta\rho$ is the difference between the mantle density and the eroded material density, and g is the acceleration due to gravity. The D parameter is solved by (Watts, 2001):

$$D = \frac{E{T_e}^3}{(1-\upsilon^2)} \quad (11)$$

We solved the model in the spectral domain, using inverse and forward Fourier Transforms to alternate between the spatial and spectral domains.

We used a locally calibrated effective thickness, T_e, of 5 km from the gravity and flexure modeling work of Peterson and Roy (2005) and assumed spatially consistent T_e across the study area. We attempted independently calibrating effective elastic thicknesses for this work by fitting the pattern of footwall topography using a broken-plate flexural approximation, but, through both brute force and Bayesian inversion techniques, we found T_e values (~2 km) (Figure S4). This effective elastic thickness is low but comparable to values reported in several other extensional settings (Armijo et al., 1996; Goren et al., 2014; Gallen and Fernández-Blanco, 2021). The other inputs into the flexural isostatic model are a mantle density of 3300 kg m^{-3}, a glacial ice density of 920 kg m^{-3}, a Young's modulus of 70 GPa, and a Poisson's ratio of 0.25. Flexural response modeling was completed using Matlab functions after Gallen and Thigpen (2018). To ensure that the model result is not affected by edge effects, we extended the model domain approximately 60 km NW of the study area, ~80 km SE of the study area, and 95 km on either side of the fault.

To mimic a broken plate segment for the fault, we modeled loads on either side of the fault independently and did not allow the flexural signal from nodes on one side of the fault to communicate to nodes on the other side of the fault. This is similar to Foster et al.'s (2010) approach, but we additionally mirrored each load on either side of the fault (Figure S5). By doing this, edge effects at the fault location are eliminated, which erroneously dampens the deflection at the fault (Figure S4). While imperfect, this model design enables a reasonable approach to simulate the broken segment of the plate. This procedure was done by importing each reconstructed load as a raster into ArcGIS and then creating duplicates of each raster to manipulate its placement in a mirrored reflection across the regional orientation of the Sangre de Cristo fault. Using the Mirror, Rotate, and Shift tools in ArcGIS, we created a reflected raster of each load across the fault, then used the Mosaic to New Raster tool to merge the minored load with the original load, resulting in a combined raster with both the original and reflected data. This raster was input into the isostasy model, and we only recorded the flexural response on the side of the fault with the original load. This approach serves to eliminate the rounding that occurs when the load is not mirrored (Figure S5A,B), creating a discontinuous boundary that is expected for a normal fault (Figure S5C,D).

Fault Mapping and Scarp Offsets

We mapped the fault at the 1:4,400 scale utilizing the USGS 3DEP lidar product, which was available at a 1 m-resolution for the study area. We additionally created hillslope, slope, and curvature maps to further enhance any signature of a fault scarp not visible solely through the lidar. Each identified fault strand was mapped in ArcGIS Pro, and given seven attributes: an identifier, a type (fault or lineament), an origin (tectonic, fluvial, questionable), identification confidence (certain, questionable, uncertain), measurability (measurable or unmeasurable), mapping confidence (certain, inferred, concealed), and any relevant notes (such as fluvially or anthropogenically modified). In total, 980 fault strands were identified throughout the mapping process, including the Villa Grove Fault Zone group of fault scarps (Figures 1C, 2A, & 3C).

We conducted two field surveys in August and October of 2022 to determine if using a kinematic GPS would further refine the fault scarp profiles. We completed 27 transects across 14 scarps in August. When reviewing the data, it was clear that due to the increased vegetation in the central and southern parts of the study area, the high-resolution kinematic GPS could not adequately penetrate the vegetative cover, resulting in erroneous transect data (Figure S6). To further determine the accuracy of this reasoning, we conducted a follow-up field visit in October to verify that vegetation was causing issues and not human error. During this excursion, we completed 14 transects across 7 scarps. Based on the results from this field excursion, it was clear that the vegetation was inhibiting the accuracy of the readings and that this method of data collection would not be as accurate as using the USGS 3DEP LiDAR data. Although this was a helpful set of trips to the field site to get a sense of the size of the scarps and the state of diffusion (e.g. degradation), they exhibited, this method did not produce fruitful results for the purposes of this analysis.

We developed a Matlab tool to measure the fault offsets along perpendicular profiles in the 1 m LiDAR data (Figure S7). The tool allows us to first load in the raster of the area of interest and draw transect profiles normal to the fault scarp strike. With the profile drawn, we fit linear regressions through the upper and lower ramps of the scarp, then identify the midpoint of the scarp to calculate the vertical separation at that point with 95% uncertainty. After the vertical separation is calculated, the user can input a quality ranking. We used a scale of 1–5 to rank the quality of the offset measurements recorded. The tool saves the location data, offset data, quality ranking, and linear regression data into an Excel file. We only used offset data that were ranked a 4 or 5 for the quality ranking to ensure only the most accurate data were used. The final dataset for the analysis of the fault scarp offset included 579 profiles on 180 individual fault scarps.

We convert scarp vertical separation, Δz, to scarp offset, S_z, following Caskey (1995). This calculation uses the surface slope of the alluvial fan, θ_f, and fault dip angle, δ, to make a geometric correction to more accurately calculate fault throw, where scarp offset is a proxy for throw (Figure S8):

$$S_z = \frac{\Delta z}{(1 - cot\delta \; tan\theta_f)} \qquad (11).$$

As shown by Hampel et al. (2021), this correction becomes more important for fans with high surface slopes. For this calculation, we measure Δz and θ_f and associated one standard deviation uncertainties from each topographic profile extracted from the lidar (e.g., Figure 3D), and we assume a range of fault dips from 55° to 65°. We calculate S_z and propagate uncertainties in all measured and assumed values using a Monte Carlo routine.

To associate the age of the fault scarps, we assigned each fault scarp to the mapped alluvial fan it cuts, as mapped by Ruleman and Brandt (2021) (Figure 3C). This map specifies the surficial geology at a scale of 1:75,000, which is considerably larger than the scale of the fault mapping, which could introduce a degree of inaccuracy in the age estimates. Although the scale is not ideal for this analysis, this is the most accurate and up-to-date map of the area at the time of this research. The relevant units for the purposes of this study included: Qa, Qac, and Qls units that spanned the Holocene (0 – 11.7 ka); Qai, Qay, Qtb, and Qtp, units that were associated with the late Pleistocene (11.7 – 129 ka) and late-to-mid Pleistocene (11.7 – 744 ka); Qao, Qao2, Qao3, and Qtpb units that were associated with mid-Pleistocene (129 ka – 774 ka) and mid-to-early Pleistocene (129 – 2588 ka); and R (undifferentiated bedrock) that we assume represent offset since at least the early Pleistocene (744 – 2588 ka). To calculate conservative estimates of fault slip rates, we divided the average offset magnitudes by the age associated with the alluvial unit in which the fault scarp was mapped. We used 11.7 ka for faults found in Holocene units, 25 ka for the late Pleistocene, as it is assumed they were last active during the LGM, and late-to-mid Pleistocene offsets, 129 ka for mid-Pleistocene and mid-to-early-Pleistocene offsets, and 774 ka for the early Pleistocene offsets assumed in the bedrock. These values were chosen to estimate the slowest possible rates for the Holocene and compare them to the highest possible rates for the Middle and Middle-to-Early Pleistocene to conservatively explore the idea of faster slip during the postglacial period (i.e., post-LGM).

Supplementary Figures:

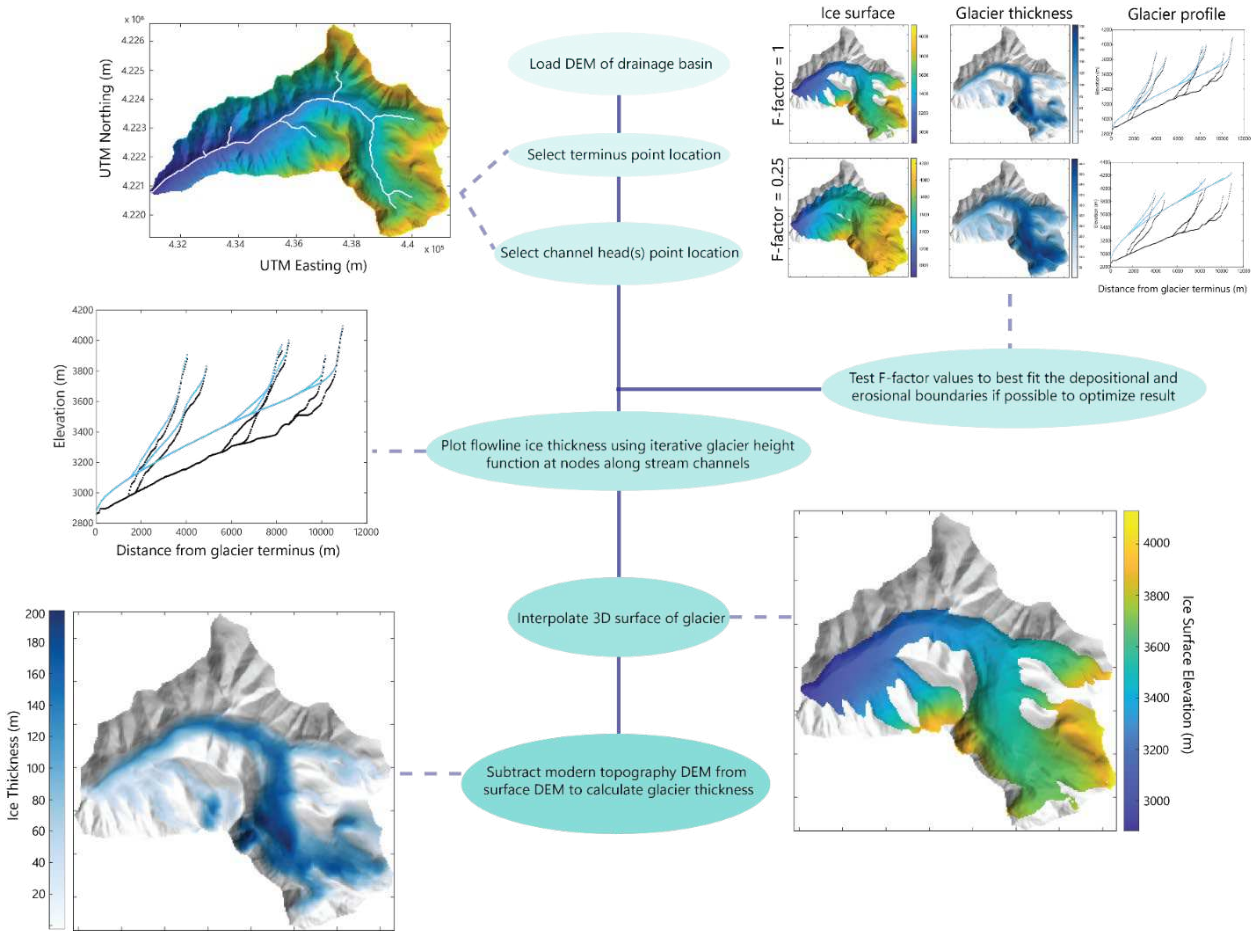

Figure S1: Schematic showing simplified glacial extent reconstruction via GlaRe process in tandem with TopoToolbox v2 functionality in Matlab. For a detailed visualization of the F-factor value rationale, see supplementary figure S2.

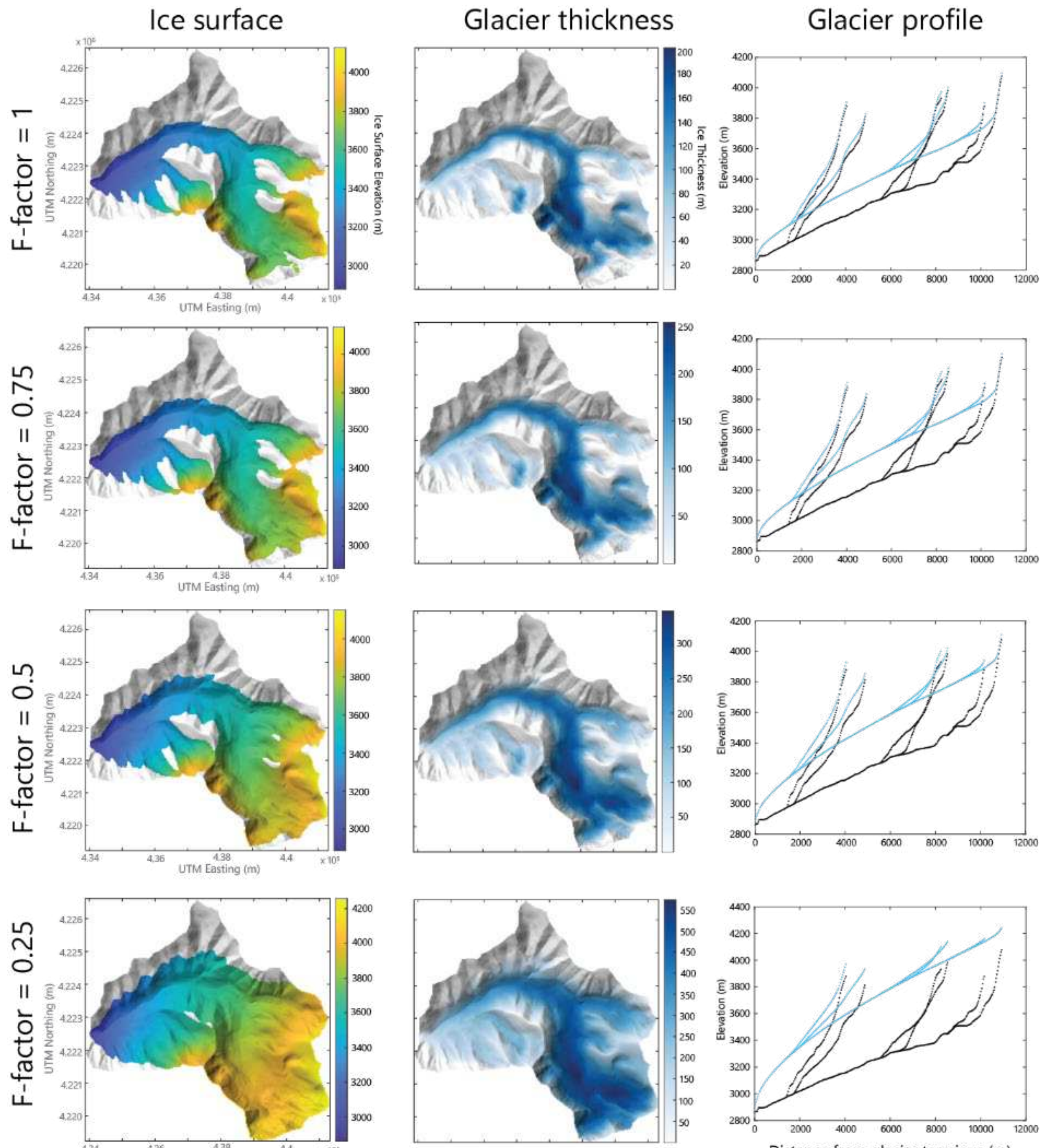

Figure S2: An example from Cotton Creek of the influence of the F-factor on paleo-glacier reconstructions. F-factor decreases from top to bottom. Glacier elevations are shown in the left columns, glacier thicknesses are shown in the middle columns, and profile reconstructions with blue lines indicating glacier elevation and black lines indicating modern topography in right columns.

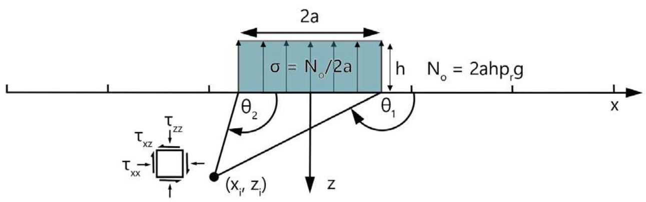

Figure S3: Diagram of the stress modeling using line loads for stress change estimation. Modified from Jeager et al. (2009).

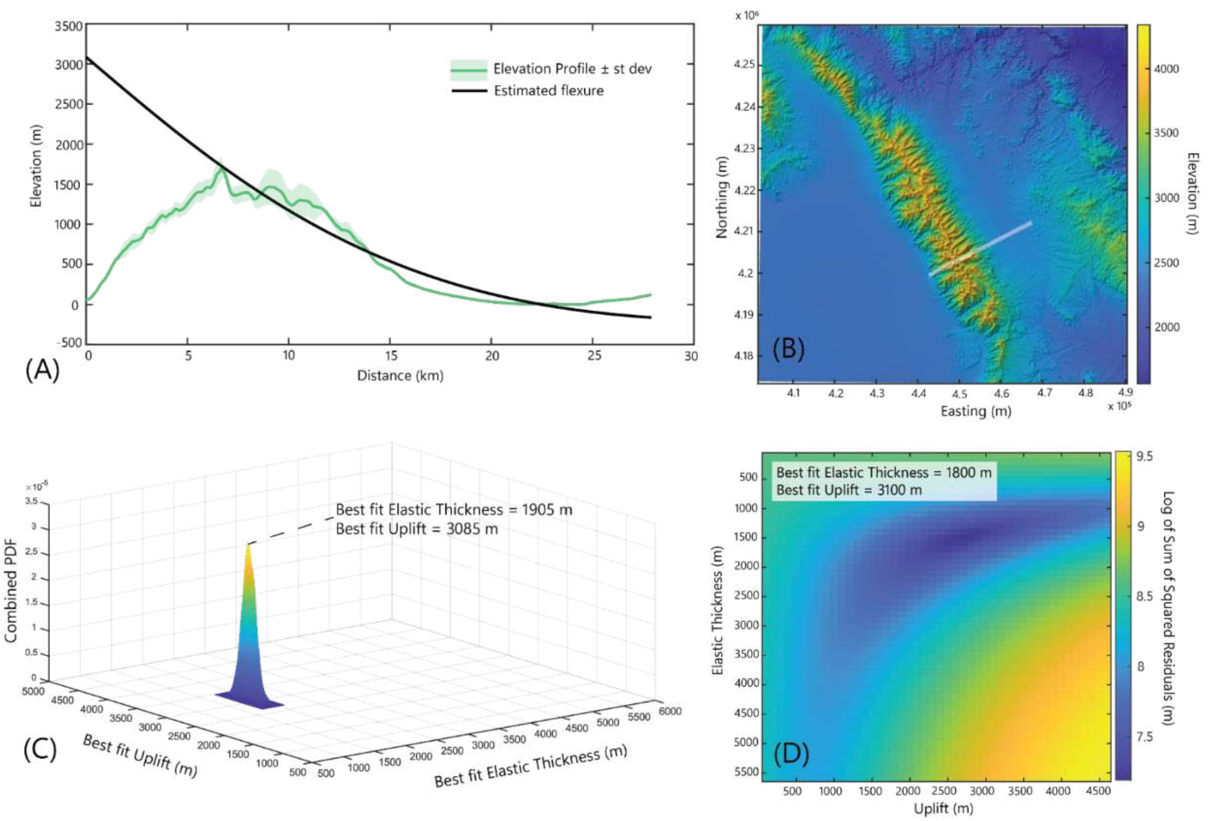

Figure S4: Calculation of calibrated effective elastic thickness (T_e) based on topographic flexure. (A) Elevation profile with our estimated flexural profile. (B) Location of elevation swath used for calculations. (C) Results of the best fit T_e and Uplift magnitudes via Bayesian inversion calculations. (D) The best fit area is in dark blue for brute force calculations.

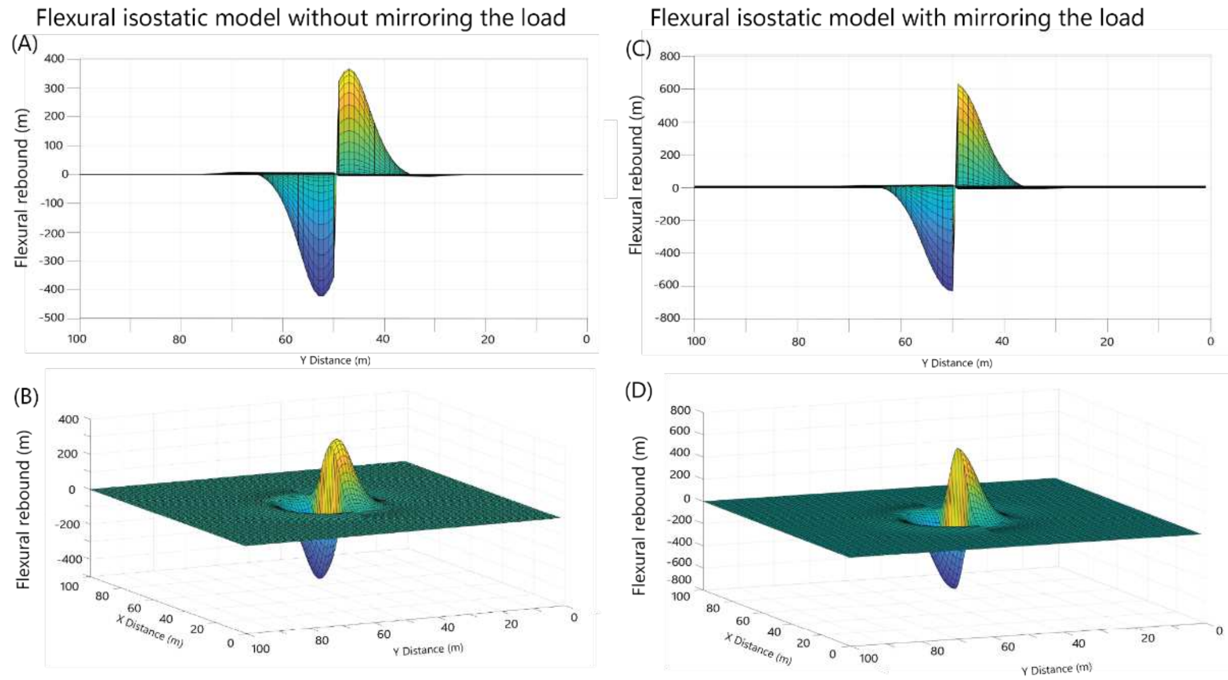

Figure S5: Broken plate isostatic model framework. Elastic half-space model without mirroring the load in (A) and (B), and with mirroring the load in (C) and (D). Note the difference in curvature of the rebound at the maxima and minima near the 'fault' break.

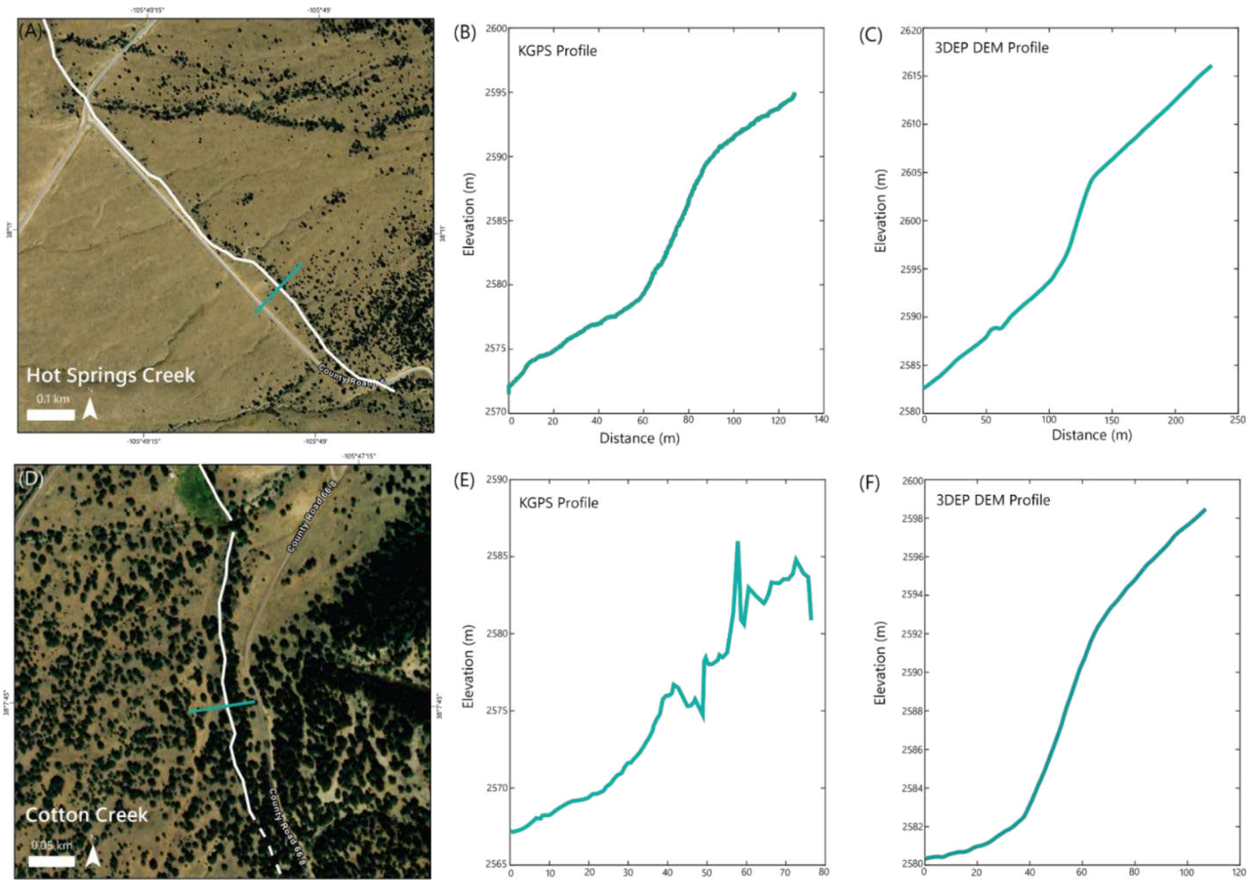

Figure S6: Comparison of scarp profile processes with Hot Springs Creek (A) as a less heavily vegetated scarp and Cotton Creek (D) as a more heavily vegetated scarp. (B) Scarp profile near Hot Springs Creek with the kinematic GPS profile taken in the field and (C) the 1 m-resolution 3DEP digital elevation model profile done in Matlab. (E) Scarp profile near Cotton Creek with the kinematic GPS profile taken in the field and (F) the 1m-resolution 3DEP digital elevation model profile done in Matlab.

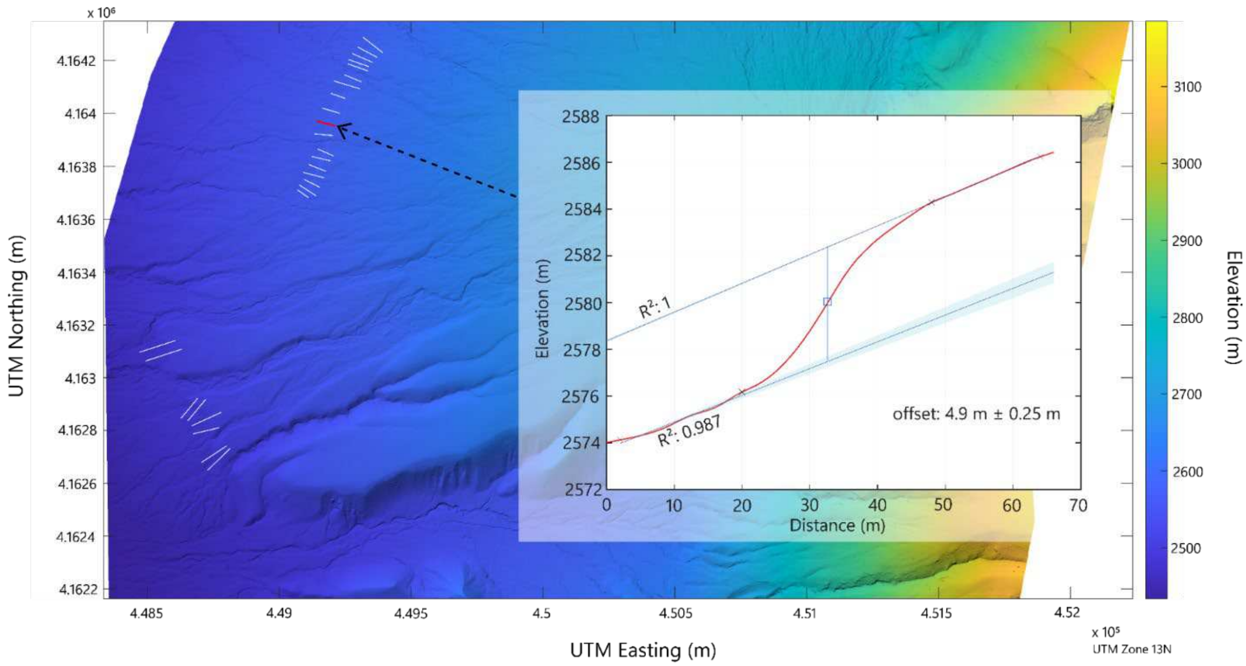

Figure S7: Example of offset measuring tool. Background: DEM overview map showing selected profiles for a round of profile measurements. Inset: scarp profile example with linear regressions on upper and lower ramps of scarp, midpoint selected at the center of the scarp, and the offset calculation with uncertainty shaded.

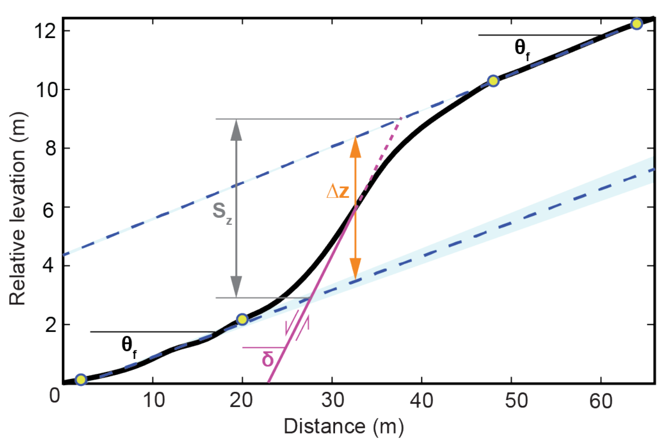

Figure S8: A scarp topographic profile from the Sangre de Cristo Mountains (black line) with fan slope, θ_f, regressions above and below fault scarp (dashed blue lines). The orange line with arrows shows the measured scarp vertical separation, Δz. A fault of a given dip, δ, is schematically shown as the purple line. This schematic (after Caskey, 1995 and Hampel et al., 2021) shows that a geometric correction is needed to accurately determine the fault vertical offset, S_z, which best approximates fault throw (Eq. 11).

References:

Amos, C.B., Audet, P., Hammond, W.C., Bürgmann, R., Johanson, I.A., and Blewitt, G., 2014, Uplift and seismicity driven by groundwater depletion in central California: Nature, v. 509, p. 483–486, doi:10.1038/nature13275.

Armijo, R., Meyer, B., King, G.C.P., Rigo, A., and Papanastassiou, D., 1996, Quaternary evolution of the Corinth Rift and its implications for the Late Cenozoic evolution of the Aegean: Geophysical Journal International, v. 126, p. 11–53, doi:10.1111/j.1365-246X.1996.tb05264.x.

Bell, J., 2020, Seismic Activity in the Northern Sangre De Cristo Fault Zone [M.S.]: University of Colorado at Boulder, 61 p., https://www.proquest.com/docview/2420687477/abstract/2FC2127267CA4E67PQ/1 (accessed March 2024).

Benn, D.I., and Hulton, N.R.J., 2010, An ExcelTM spreadsheet program for reconstructing the surface profile of former mountain glaciers and ice caps: Computers & Geosciences, v. 36, p. 605–610, doi:10.1016/j.cageo.2009.09.016.

Bennett, M.M., and Glasser, N.F. (Eds.), 2009, Glacial Geology: Ice Sheets and Landforms: Chichester, UK ; Hoboken, NJ, Wiley, 400 p.

Caskey, S.J., 1995, Geometric relations of dip slip to a faulted ground surface: new nomograms for estimating components of fault displacement: Journal of Structural Geology, v. 17, p. 1197–1202, doi:10.1016/0191-8141(95)00023-7.

Doser, D.I., and Smith, R.B., 1989, An assessment of source parameters of earthquakes in the cordillera of the western United States: Bulletin of the Seismological Society of America, v. 79, p. 1383–1409, doi:10.1785/BSSA0790051383.

Foster, D., Brocklehurst, S.H., and Gawthorpe, R.L., 2010, Glacial-topographic interactions in the Teton Range, Wyoming: Journal of Geophysical Research: Earth Surface, v. 115, doi:10.1029/2008JF001135.

Gallen, S.F., and Fernández-Blanco, D., 2021, A New Data-Driven Bayesian Inversion of Fluvial Topography Clarifies the Tectonic History of the Corinth Rift and Reveals a Channel Steepness Threshold: Journal of Geophysical Research: Earth Surface, v. 126, p. e2020JF005651, doi:10.1029/2020JF005651.

Gallen, S.F., and Thigpen, J.R., 2018, Lithologic Controls on Focused Erosion and Intraplate Earthquakes in the Eastern Tennessee Seismic Zone: Geophysical Research Letters, v. 45, p. 9569–9578, doi:10.1029/2018GL079157.

Goren, L., Fox, M., and Willett, S.D., 2014, Tectonics from fluvial topography using formal linear inversion: Theory and applications to the Inyo Mountains, California: Journal of Geophysical Research: Earth Surface, v. 119, p. 1651–1681, doi:10.1002/2014JF003079.

Hampel, A., Hetzel, R., and Erdmann, M.-S., 2021, Postglacial slip distribution along the Teton normal fault (Wyoming, USA), derived from tectonically offset geomorphological features: Geosphere, v. 17, p. 1517–1533, doi:10.1130/GES02370.1.

Jaeger, J., Cook, N.G., and Zimmerman, R., 2007, Fundamentals of Rock Mechanics: Malden, MA, Wiley-Blackwell, 488 p.

Jiskoot, H., 2011, Dynamics of Glaciers, *in* Singh, V.P., Singh, P., and Haritashya, U.K. eds., Encyclopedia of Snow, Ice and Glaciers, Dordrecht, Springer Netherlands, Encyclopedia of Earth Sciences Series, p. 245–256, doi:10.1007/978-90-481-2642-2_127.

Pellitero, R., Rea, B.R., Spagnolo, M., Bakke, J., Ivy-Ochs, S., Frew, C.R., Hughes, P., Ribolini, A., Lukas, S., and Renssen, H., 2016, GlaRe, a GIS tool to reconstruct the 3D surface of palaeoglaciers: Computers & Geosciences, v. 94, p. 77–85, doi:10.1016/j.cageo.2016.06.008.

Peterson, C., and Roy, M., 2005, Gravity and flexure models of the San Luis, Albuquerque, and Tularosa basins in the Rio Grande rift, New Mexico, and southern Colorado, *in* Geology of the Chama Basin, New Mexico Geological Society, p. 105–114, doi:10.56577/FFC-56.105.

Pierce, K.L., 1979, History and dynamics of glaciation in the northern Yellowstone National Park area: US Geological Survey Professional Paper, doi:10.3133/pp729F.

Ruleman, C.A., and Brandt, T.R., 2021, Surficial geology of the northern San Luis Valley, Saguache, Fremont, Custer, Alamosa, Rio Grande, Conejos, and Costilla Counties, Colorado: U.S. Geological Survey Scientific Investigations Map 3475, 2 sheets, doi:10.3133/sim3475.

Schilling, D., and Hollin, J.T., 1981, Numerical reconstructions of valley glaciers and small ice caps, *in* Denton, G.H. and Hughes, J.T. eds., The Last Great Ice Sheets, New York, Wiley, p. 207–220.

Watts, A.B., 2001, Isostasy and Flexure of the Lithosphere: Cambridge University Press, 508 p.